

Solar Orbiter Observations of the Kelvin-Helmholtz Instability in the Solar Wind

R. Kieokaew¹, B. Lavraud^{1,2}, Y. Yang³, W. H. Matthaeus⁴, D. Ruffolo⁵, J. E. Stawarz⁶, S. Aizawa¹, C. Foullon⁷, V. Génot¹, R. F. Pinto^{1,8}, N. Fargette¹, P. Louarn¹, A. Rouillard¹, A. Fedorov¹, E. Penou¹, C.J. Owen⁹, T. Horbury⁶, H. O'Brien⁶, V. Evans⁶, and V. Angelini⁶

¹Institut de Recherche en Astrophysique et Planétologie, CNRS, UPS, CNES, 9 Ave. du Colonel Roche 31028 Toulouse, France
e-mail: rkieokaew@irap.omp.eu

²Laboratoire d'Astrophysique de Bordeaux, Univ. Bordeaux, CNRS, B18N, allée Georoy Saint-Hilaire, 33615 Pessac, France

³Department of Mechanics and Aerospace Engineering, Southern University of Science and Technology, Shenzhen 518055, People's Republic of China

⁴Department of Physics and Astronomy and Bartol Research Institute, University of Delaware, Newark, DE 19716, USA

⁵Department of Physics, Faculty of Science, Mahidol University, Bangkok 10400, Thailand

⁶Space and Atmospheric Physics, Department of Physics, Blackett Laboratory, Imperial College London, London, UK SW7 2AZ

⁷CGAFD, Mathematics, CEMPS, University of Exeter, Exeter, UK

⁸LDE3, DAp/AIM, CEA Saclay, 91191 Gif-sur-Yvette, France

⁹Department of Space and Climate Physics, University College London, Mullard Space Science Laboratory, Holmbury St. Mary, RH5 6NT, UK.

Received September 15, 1996; accepted March 16, 1997

ABSTRACT

Context. The Kelvin-Helmholtz instability (KHI) is a nonlinear shear-driven instability that develops at the interface between shear flows in plasmas. KHI has been inferred in various astrophysical plasmas, and has been observed in situ at the magnetospheric boundaries of solar-system planets and through remote sensing at the boundaries of coronal mass ejections.

Aims. KHI is also expected to develop at flow shear interfaces in the solar wind. While it was hypothesized to play an important role in the mixing of plasmas and in triggering solar wind fluctuations, its direct and unambiguous observation in the solar wind was still lacking.

Methods. We report in-situ observations of ongoing KHI in the solar wind using Solar Orbiter during its cruise phase. The KHI is found in a shear layer in the slow solar wind in the close vicinity of the Heliospheric Current Sheet, with properties satisfying linear theory for its development. Analysis is performed to derive the local configuration of the KHI. A 2-D MHD simulation is also set up with the empirical values to test the stability of the shear layer. In addition, magnetic spectra of the KHI event are analyzed.

Results. We find that the observed conditions satisfy the KHI onset criterion from the linear theory analysis, and its development is further confirmed by the simulation. The current sheet geometry analyses are found to be consistent with KHI development. Additionally, we report observations of an ion jet consistent with magnetic reconnection at a compressed current sheet within the KHI interval. The KHI is found to excite magnetic and velocity fluctuations with power law scalings that approximately follow $k^{-5/3}$ and $k^{-2.8}$ in the inertial and dissipation ranges, respectively. Finally, we discuss reasons for the lack of in-situ KHI detection in past data.

Conclusions. These observations provide robust evidence of KHI development in the solar wind. This sheds new light on the process of shear-driven turbulence as mediated by the KHI with implications for the driving of solar wind fluctuations.

Key words. Solar-wind shear flows – Kelvin-Helmholtz instability – Slow solar-wind – Heliosphere – Space plasmas

1. Introduction

The magnetic Kelvin-Helmholtz instability (KHI) is a magnetohydrodynamic (MHD) shear-driven instability frequently observed in solar system plasmas. KHI can be induced at the surface between two media with different flow velocity and plasma conditions. This shear instability is fundamental and can be found in many flow shear systems throughout the Universe. The KHI that has been most studied in situ is at the Earth's magnetopause and low-latitude boundary layers where periodic fluctuations of magnetic fields and plasma parameters are observed (e.g., Hones et al. 1981; Fairfield et al. 2000; Hasegawa et al. 2004; Foullon et al. 2008; Eriksson et al. 2016). This is because the Earth's flank magnetopause is prone to the KHI onset condition which prefers weak magnetic field in the direction of the

shear flow. Nevertheless, KHI has been observed in strong magnetic field environments such as in the solar corona (Ofman & Thompson 2011) and at the flank of a coronal mass ejection (CME) (e.g., Foullon et al. 2011; Foullon et al. 2013; Möstl et al. 2013) via Extreme Ultraviolet (EUV) imaging by the Solar Dynamics Observatory (SDO). Variations of the KHI such as a sinusoidal mode have also been observed in a solar prominence (Hillier & Polito 2018) using Interface Region Imaging Spectrograph (De Pontieu et al. 2014).

Recently, remote observations above the solar corona using Heliospheric Imager instrument on board the Solar-Terrestrial Relations Observatory (STEREO/HI1) have revealed a transition in texture of the solar wind from highly anisotropic coronal plasma, or “striae”, to more isotropic, or “flocculated”, solar-wind plasma (DeForest et al. 2016). The transition is found to

be consistent with the onset of hydrodynamic and MHD instabilities leading to development of turbulence. Qualitatively, this transition is found to occur near the first surface of plasma $\beta = 1$, where the β changes from $\beta \ll 1$ near the Sun to $\beta \approx 1$, and the Alfvén critical surface where the solar wind speed reaches the Alfvén speed ($V = V_A$) (Chhiber et al. 2018). Ruffolo et al. (2020) propose that the transition from striae to flocculation of the young solar wind is powered by shear-driven instabilities such as the KHI, caused by the relative velocities of adjacent coronal magnetic flux tubes. This is supported by compressible MHD numerical simulations in which several features observed by Parker Solar Probe (PSP; Fox et al. 2016) including the magnetic “switchback” signatures near perihelia are reproduced. It is argued that the KHI can be triggered when the relative velocity between flux tubes is larger than the local Alfvén velocity ($\Delta V > V_A$) when the magnetic field is along the velocity shear, leading to shear-driven turbulence just outside the Alfvén critical zone.

In theory, the KHI may develop at tangential discontinuities (TDs) because there are relative changes in velocity field (\mathbf{V}) and magnetic field (\mathbf{B}) across them and no normal magnetic field threading through them, which would otherwise stabilize the instability (as for rotational discontinuities). The solar wind is full of TDs (e.g., Burlaga et al. 1977; Knetter et al. 2004; Neugebauer & Giacalone 2010), which separate different plasma regions. TDs are thought of as surfaces that separate adjacent solar wind flux-tubes (e.g., Hollweg 1982) that originated from granules, or meso/super granules in the Sun’s photosphere (e.g., Roudier & Muller 1986; Axford & McKenzie 1992) with different plasma properties and composition and spread out in the heliosphere (e.g., Bruno & Carbone 2005; Borovsky 2008). It was demonstrated theoretically by many authors that TDs can support MHD surface waves (e.g., Hollweg 1982). In particular, TDs could support the KHI (e.g., Burlaga 1972; Neugebauer et al. 1986). As for the flux tube picture, it was suggested that the KHI should be induced when adjacent flux tubes move relative to each other with a speed greater than the Alfvén speed (Burlaga 1972). Zaqarashvili et al. (2014) consider the topology of magnetic flux tubes and found that, while the axial \mathbf{B} of the flux tubes stabilizes the KHI, a slight twist in the \mathbf{B} (i.e., as for when the \mathbf{B} does not align with the \mathbf{V}) may allow the surface between them with $\Delta V < V_A$ to become unstable to the KHI.

Across TDs, an alignment between the change in velocity (ΔV) and the change in magnetic field (ΔB) are commonly observed (Neugebauer 1985; Neugebauer et al. 1986; Neugebauer 2006; Knetter et al. 2004). This alignment is not expected from the MHD discontinuity theory, unlike at rotational discontinuities where this alignment is expected (Hudson 1970). This alignment of ΔV and ΔB is observed independent of the type of solar wind stream between 1 and 2.2 AU based on IMP 8 and Voyager 2 data (Neugebauer 1985). Based on Helios data, Neugebauer et al. (1986) report that this alignment is also observed as close as 0.3 AU. They further consider the possibility that the KHI may have developed across TDs and destroyed the random alignment between ΔV and ΔB . Since the number of TDs per unit time decrease with distance from the Sun (e.g., Tsurutani & Smith 1979; Lepping & Behannon 1986), Neugebauer et al. (1986) suggested that the KHI may have destroyed TDs as the KHI growth rate becomes larger with decreasing Alfvén speed.

Despite all these postulations, the KHI has not been observed in situ in the solar wind to our knowledge. Here we report unambiguous in-situ KHI detection in Solar Orbiter observations (SolO; Müller et al. 2020) during its cruise phase. SolO

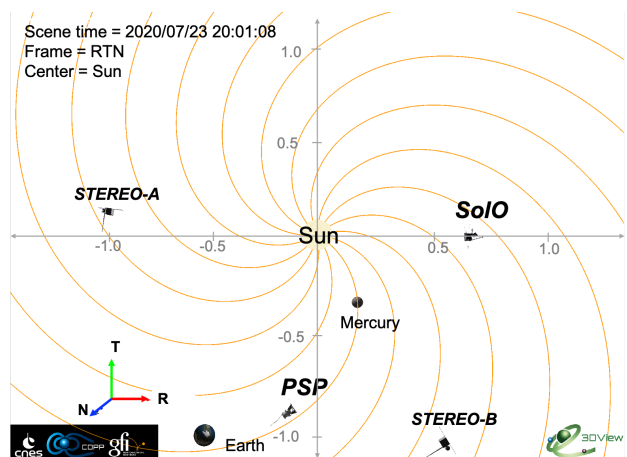


Fig. 1. Overview of SolO and other spacecraft positions on 23 July 2020 at 20:01:08 UT in the RTN coordinates. Orange solid lines represent solar wind Parker spirals (Parker 1958) calculated using a constant velocity of 300 km s^{-1} . This figure was obtained using the 3DView software (Génot et al. 2018).

is an ESA mission, launched on February 10, 2020, aimed to study the Sun and inner heliosphere from out-of-ecliptic vantage points. The cruise phase started in June 2020 with the in-situ instruments operated nominally after a successful commissioning. SolO was at 0.69 AU during the observations presented here when several periodic fluctuations in plasma parameters are observed.

In this work, we report quasi-periodic magnetic and plasma variations within a shear layer in the slow solar wind consistent with the development of the KHI, supported by the linear theory analysis and numerical simulations. The paper is organized as follows. First, we present the instrumentation and overview, context, and KHI observations in Section 2. Additionally, we report observations of magnetic reconnection signatures in the KHI. Then, we focus on the linear theory, boundary layer analyses, numerical simulations, and magnetic spectra of the KHI in Section 3. As this event shows clear evidence of the KHI in the solar wind, we discuss why it was not observed in past data, as well as its implications for solar wind dynamics in Section 4. We summarize our findings and discussion in Section 5.

2. Observations

2.1. Instrumentation and overview

We use magnetic field data from the fluxgate vector magnetometer (MAG; Horbury et al. 2020). MAG continuously samples the magnetic field with the rate up to 16 vector/s in the normal mode and up to 128 vector/s in the burst mode with a precision of about 5 pT. We also use particle data from the Proton and Alpha Particle Sensor (PAS) that is part of the Solar Wind Analysis instrument suite (SWA; Owen et al. 2020). PAS provides high-cadence measurements of 3D velocity distribution function of solar wind particles (electrons, protons, alpha particles, and heavy ions). We use the Radial Tangential Normal (RTN) coordinate system throughout this paper unless stated otherwise. In this system, the coordinates are centred at the spacecraft where R is directed radially outward from the Sun to spacecraft, T is longitudinal along the cross product of the Sun’s rotation vector with R , and N completes the right-handed orthogonal set, which points in the latitudinal direction.

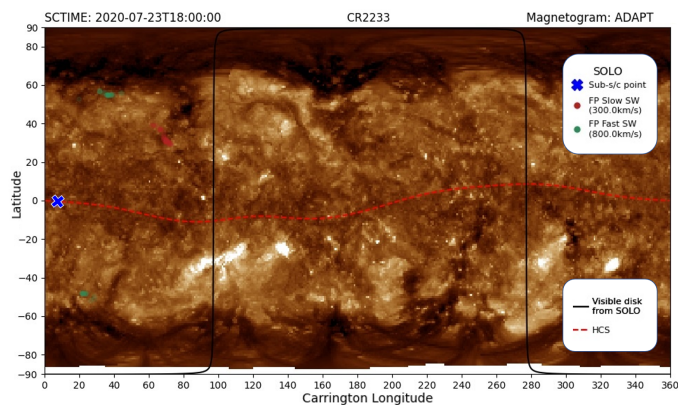


Fig. 2. Connectivity map of the observations on July 23, 2020, produced from the Connectivity Tool (Rouillard et al. 2020) to provide a global context. The background image is a combined image from remote observation using SDO/AIA and STEREO-A/EUVI 193 Å Carrington maps. The SoLo position is projected to the area of observation and is shown as a blue cross (see text). The Heliospheric Current Sheet (HCS) is marked with a red dashed line.

On July 23 - 24, 2020, SoLo was at the distance 0.69 AU from the Sun. From July 23 at 12:00 UT to July 24 at 12:00 UT, SoLo was moving from the distance $r = 1.03 \times 10^8$ km (0.68 AU) to $r = 1.04 \times 10^8$ km (0.70 AU) from the Sun. Fig. 1 shows the projected position of SoLo onto the equatorial plane with the solar wind Parker spiral (orange lines) (Parker 1958) calculated using a constant solar wind speed of 300 km s^{-1} . This figure is obtained using the 3DView software (Génot et al. 2018) available at <http://3dview.cdpp.eu/>. The radial speed of SoLo was $V_R = 11.3 \text{ km s}^{-1}$ throughout this interval.

Fig. 2 shows the global context on July 23, 2020 from 18 to 24 UT of the solar observations with the SoLo position (blue cross) projected back to the Sun’s surface. This figure is obtained from the Magnetic Connectivity Tool (Rouillard et al. 2020), accessible at <http://connect-tool.irap.omp.eu/>, that can be used to connect between remote observations and in-situ observations. The background image is produced by combining images taken by SDO and STEREO-A in EUV at 193 Å, using the Heliospheric Imagers (HI) instruments on board. The green and red dots indicate the points at the surface that are most likely to be magnetically connected to SoLo, assuming uniform slow and fast wind flows. The SoLo position is estimated to be at the blue cross position. The connected positions are projected on magnetograms from the ADAPT (Air Force Data Assimilative Photospheric Flux Transport) flux transport model (Arge et al. 2010; Hickmann et al. 2015). On this image, the SoLo position appears at low-latitude ($\sim 0^\circ$) and near the Heliospheric Current Sheet marked by a red dashed line. In this work, we report SoLo observations of the KHI near an edge of the HCS.

2.2. 12-hour context

Fig. 3 shows SoLo observations between 16:00 UT on July 23, 2020 and 6:00 UT on July 24, 2020, covering a 12-hour interval. In Fig. 3a, we show the magnetic field components and magnitude. Fig. 3b displays the radial component (V_R) and Fig. 3c the tangential (V_T) and out-of-ecliptic (V_N) components of the ion bulk flow velocity. Two main HCS crossings are observed between 22:00 UT on July 23 and 2:00 UT on July 24 in between the purple vertical dotted lines. The HCS is characterized by a large-scale (\sim several hours) change in the polarity of the ra-

dial magnetic field (B_R). Around 18:00 UT on July 23, we mark a meso-scale structure (\sim a few hours) between vertical orange dotted lines, characterizing bipolar magnetic fields with a sharp magnetic transition (i.e., current sheet) at the center. At this central current sheet, there is an ion jet clearly seen in V_R and V_N , probably indicating ongoing magnetic reconnection. This structure is known as Magnetic Increase with Central Current Sheet (MICCS) and it has been observed with Parker Solar Probe (Fargette et al. 2021); this signature corresponds to two magnetic flux tubes that become interlinked and with magnetic reconnection at the interface (e.g., Louarn 2004; Kacem et al. 2018; Øieroset et al. 2019; Kieokaew et al. 2020). Although mentioned here for context, this feature is not discussed any more in our study.

From 20:45 to 21:30 UT on July 23 in Fig. 3c, we observe a velocity shear of about 30 km s^{-1} in the V_T (green) and about 20 km s^{-1} in the V_N (blue) components. This velocity shear interval features periodic fluctuations in the magnetic fields (Fig. 3a) and the radial velocity (V_R ; Fig. 3b). The shear layer is also accompanied by changes in the ion number density shown in Fig. 3d. This interval as shaded in grey exhibits KH-like signatures; we show a zoom-in of this interval in the next section.

Figs. 3e, 3f, and 3g show the Alfvén Mach number (M_A), the normalized cross-helicity (σ_c), and the angle between \mathbf{V} and \mathbf{B} changes (θ_{VB}), respectively. During the shaded interval, the M_A is 12, indicating that the solar wind is super-Alfvénic. The σ_c (Matthaeus & Goldstein 1982; Roberts et al. 1992) is calculated from $\sigma_c = 2\langle\delta\mathbf{v}\cdot\delta\mathbf{b}\rangle/(\langle\delta\mathbf{v}\rangle^2 + \langle\delta\mathbf{b}\rangle^2)$, where $\delta\mathbf{v} = \mathbf{V} - \langle\mathbf{V}\rangle_{20min}$ and $\delta\mathbf{b} - \langle\mathbf{b}\rangle_{20min}$ are the velocity field and magnetic field fluctuations from the 20-min running averages of \mathbf{V} and $\mathbf{b} = \mathbf{B}/\sqrt{\mu_0\rho}$, where μ_0 is the vacuum permeability and ρ is the average proton mass density, respectively. The magnetic field \mathbf{b} is measured in Alfvén speed units in km s^{-1} . The sum ($\langle\rangle$) brackets are also taken over 20-min running averages. σ_c relates to the cross helicity $H_c = \frac{1}{2} \int (\mathbf{V} \cdot \mathbf{b}) d^2x$ and the energy per unit mass $E = \frac{1}{2} \int (\mathbf{V}^2 + \mathbf{b}^2) d^2x$ through the relation $\sigma_c = 2H_c/E$. This quantity measures the Alfvénicity with $\sigma_c = \pm 1$ indicating Alfvénic fluctuations, where the signs $+$, $-$ correspond to Alfvénic propagation anti-parallel or parallel to the mean field, respectively. During the shaded interval, σ_c is fluctuating around 0.5, indicating that the solar wind is not strongly Alfvénic. The angle θ_{VB} is calculated from $\arccos(\delta\mathbf{v} \cdot \delta\mathbf{b}/(|\delta\mathbf{v}||\delta\mathbf{b}|))$. For the shaded time period, Fig. 3g shows that the angle between $\delta\mathbf{v}$ and $\delta\mathbf{b}$ is spreading from 90° to 120° . The non-alignment of $\delta\mathbf{v}$ and $\delta\mathbf{b}$ during this interval indicates the possibility for this shear layer to be unstable to the KHI. The KHI would be suppressed if the magnetic field change aligns with the velocity field change due to the magnetic tension exerted in the direction of the shear flow (e.g., Chandrasekhar 1961), i.e., when θ_{VB} is near 0° or 180° .

2.3. KHI observations

Fig. 4 shows a zoom-in around the shaded time period in Fig. 3 between 20:45 and 21:30 UT on July 23, 2020. The quasi-periodic fluctuations in several parameters resemble in-situ KH waves at the interface between shear flows (e.g., Hasegawa et al. 2004). The magnetic field in Fig. 4a clearly shows repeated, homologous fluctuations in all components. We mark sharp magnetic rotations (1) - (7) with vertical dashed lines. Fig. 4b shows V_R and Fig. 4c shows V_T and V_N components of the ion bulk velocity. The velocity shear is clearly seen in the V_T component. To mark the shear layer, we define Side 1 at 20:38 UT as the beginning of the shear interval and Side 2 as the end of the shear inter-

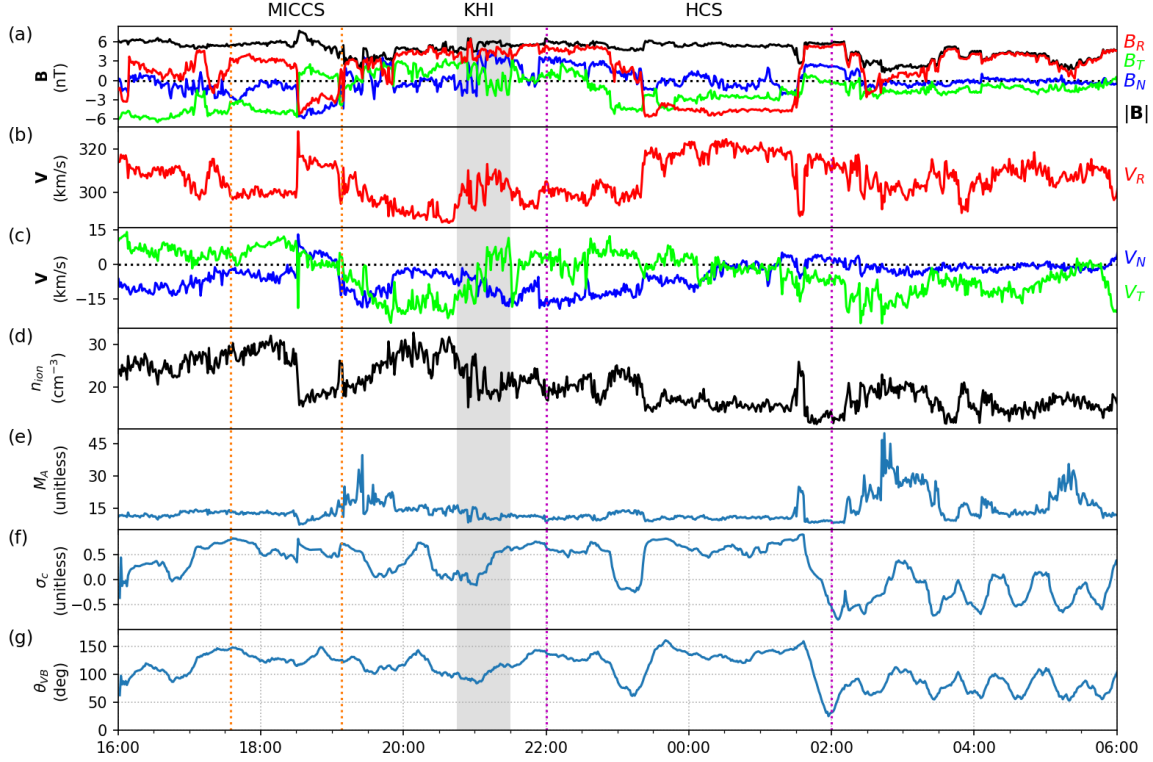


Fig. 3. Solar Orbiter observations between 16:00 UT on 23 July 2020 and 6:00 UT on 24 July 2020 showing the context of the Kelvin-Helmholtz instability observation (shaded area). (a) Magnetic fields in the RTN coordinates. (b) Ion bulk velocity V_R component. (c) Ion bulk velocity V_T and V_N components. (d) Ion number density. (e) Alfvén Mach number. (f) Normalized cross-helicity. (g) The angle between $\delta\mathbf{v}$ and $\delta\mathbf{b}$ (see text). The Heliospheric Current Sheet (HCS) is observed between 22:00 UT on 23 July 2020 and 2:00 UT on 24 July 2020, marked by purple dotted lines. The Magnetic Increase with Central Current Sheet (MICCS) is observed between 17:35 and 18:08 UT on 23 July 2020, marked by orange dotted lines.

Table 1. Timing of the KH wave edges marked in Fig. 4 and time difference between them.

Numbers	Times (UT)	Time difference (mm:ss)
(1)	20:45:59	-
(2)	20:53:43	07:44
(3)	21:02:11	08:28
(4)	21:09:56	07:45
(5)	21:17:32	07:36
(6)	21:23:39	06:07
(7)	21:29:38	05:59

val at 21:29 UT, marked by magenta dotted-dashed lines. Sides 1 and 2 are characterized by the tangential velocity V_T which reached local minimum and maximum, respectively. The periodic features are also seen in the velocity fields especially for the tangential (V_T) component in Fig. 4c in which sudden, sharp transitions collocate with the changes in the magnetic field marked by the vertical dashed lines. To facilitate discussion, we define the magnetic rotations (1) - (7) as “wave edges” that mark sudden changes in both magnetic and velocity fields. Table 1 notes times of these wave edges and time differences between these edges. These time differences correspond to the period of the waves. The average time difference between wave edges is 7 minutes 17 seconds (s) and the standard deviation is 55 s. We analyze the wave edges in detail in Section 3.3.

Fig. 4d shows Alfvén speed and Alfvén velocity components ($\mathbf{V}_A = \mathbf{B} / \sqrt{\mu_0 n_i m_p}$, where n_i is the ion number density and m_p is the proton mass). The average Alfvén speed in this interval is 26 km s^{-1} . Fig. 4e shows the ion number density (n_{ion}). Despite some fluctuations, n_{ion} gradually changes from 30 cm^{-3} at Side 1 to 22 cm^{-3} at Side 2. Fig. 4f shows the magnetic (P_m), thermal (P_p), and total pressures ($P_{tot} = P_m + P_p$). The total pressure is approximately constant, indicating approximate pressure balance across the shear layer. Fig. 4g shows the ion beta (β). The β is changing from $\beta \approx 2$ at Side 1 to $\beta \approx 1$ at Side 2. A strong peak in β of about $\beta \approx 7$ is observed adjacent to wave edge (3). At wave edge (3), there is an ion jet in V_N (blue in Fig. 4c) with $\Delta V_N \sim 11 \text{ km s}^{-1}$ that collocates with the magnetic rotation observed in B_N (blue in Fig. 4a). We explain that this ion jet may be produced by magnetic reconnection, in Section 2.4.

Table 2 summarizes the values of \mathbf{V} , \mathbf{B} and n_{ion} at Sides 1 and 2. Considering the velocity change across the shear layer, we define $\Delta\mathbf{V} = \mathbf{V}_2 - \mathbf{V}_1$, where the subscripts 1 and 2 label Sides 1 and 2, respectively. The velocity change is $\Delta\mathbf{V} = (\Delta V_R, \Delta V_T, \Delta V_N) = (30, 30, -11) \text{ km s}^{-1}$, with $|\Delta\mathbf{V}| = 44 \text{ km s}^{-1}$. The ratio of the velocity change across the shear layer to the average Alfvén speed is therefore $\Delta V/V_A = 1.7$. An important criterion of the KHI from the linear theory of stability of a shear layer in plasmas considered by Chandrasekhar (1961), Sen (1963), and Landau & Lifshitz (1960) is that the KHI would be suppressed for $\Delta V < V_A$, i.e., when the velocity shear is less than the local Alfvénic speed. Note that this condition is obtained in

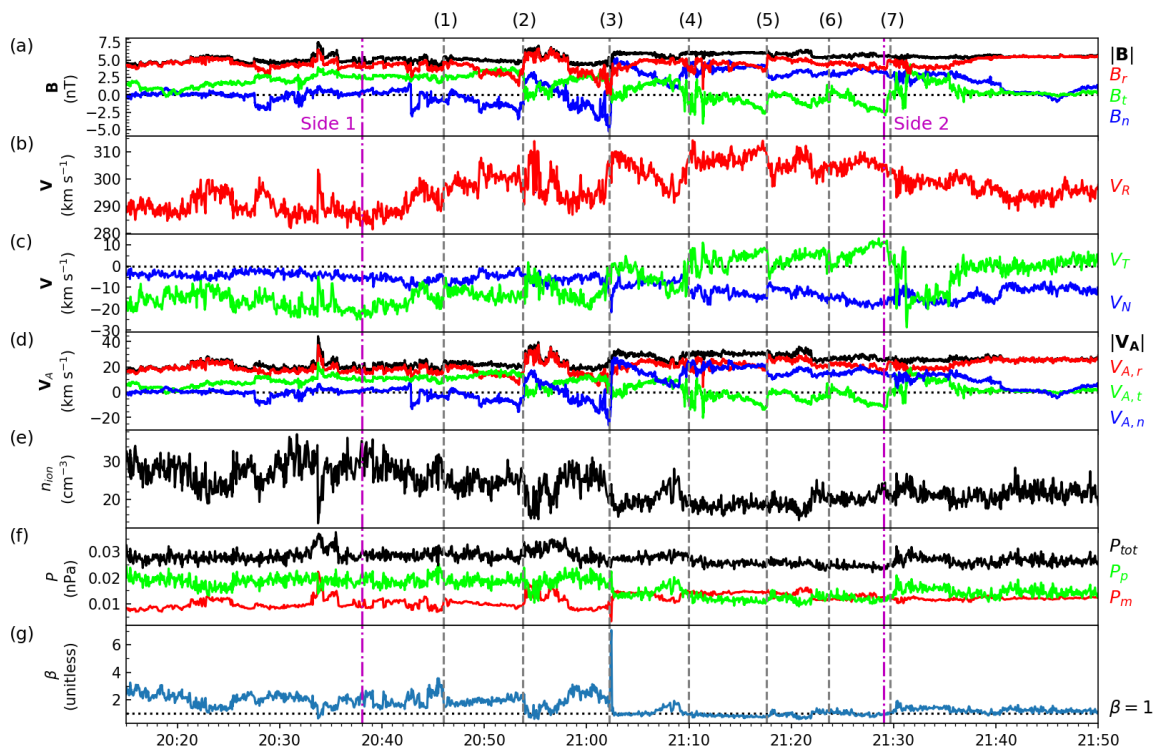


Fig. 4. Solar Orbiter observations on 23 July 2020 between 20:10 UT and 21:50 UT. (a) Magnetic field in the RTN coordinates. (b) Ion bulk velocity V_R component. (c) Ion bulk velocity V_T and V_N components. (d) Alfvén speed $|V_A|$ and Alfvén velocity components ($V_{A,r}$, $V_{A,t}$, $V_{A,n}$). (e) Ion number density. (f) Plasma pressure P_p , magnetic pressure P_m , and total pressure P_{tot} . (g) Plasma beta β . The KH waves can be noticed between 20:45 and 21:30 UT. The vertical grey dashed lines (1) - (7) mark the boundary layer crossings corresponding to KH trailing edges. The magenta dashed-dotted lines mark times when the plasma parameters reach asymptotic values on Side 1 (20:38 UT) and Side 2 (21:29 UT) of the shear layer.

Table 2. Parameter values on Side 1 and Side 2 of the shear layer marked in Fig. 4.

Parameters	Side 1	Side 2	Units
V_R	285	305	km s^{-1}
V_T	-20	10	km s^{-1}
V_N	-5	-16	km s^{-1}
B_R	4	4	nT
B_T	2	-2	nT
B_N	0	3	nT
n_{ion}	30	22	cm^{-3}

a simplistic configuration of an infinitely thin shear layer embedded in the uniform density and magnetic field and with the magnetic field being exactly along the velocity shear. The observed shear velocity exceeds the local Alfvén speed for this approximate consideration and thus the KHI is not suppressed. In Section 3.1, to test whether the observed local shear conditions support the KHI growth, we consider the KHI onset condition by taking into account the nonuniform conditions on either side of the shear layer derived from the linear theory. We also set up a local MHD simulation using these empirical conditions in Section 3.2.

2.4. Magnetic reconnection

Fig. 5 shows a zoom-in at wave edge (3) in Fig. 4 that contains an ion jet collocated with the change in magnetic field seen in the N component (blue). The current sheet interval at the wave edge is delineated by orange dashed lines between 21:02:00 and 21:02:40 UT. The magnetic field magnitude in Fig. 5a shows a drop at the centre of the current sheet of about 2.5 nT. To clearly see the ion jet, we transform the magnetic field into local current sheet LMN coordinates using the hybrid Maximum Variance Analysis (MVA) technique (Gosling & Phan 2013). In this coordinate system, L points in the magnetic shear direction (i.e., the reconnecting component), N points in the direction normal to the shear plane, and $M = N \times L$ points in the out-of-plane direction (i.e., the guide-field direction). We transform the magnetic field from the RTN coordinates to LMN coordinates as follows. First, the current sheet normal N is obtained from the cross-product of the asymptotic 10-s averaged magnetic fields just outside the current sheet interval. Second, the M component is obtained from $N \times L_1$, where L_1 is the maximum variance direction obtained from the MVA technique (Sonnerup & Cahill 1967) applied in the current sheet interval. Finally, $L = M \times N$ completes the right-handed orthonormal system. We obtain $L = [-0.285, 0.245, -0.924]$, $M = [0.882, 0.44, -0.156]$, and $N = [0.37, -0.863, -0.343]$.

The magnetic field rotation is clearly seen in the B_L component in Fig. 5b. B_L rotates from positive to negative during the current sheet interval in collocation with the ion jet seen in the

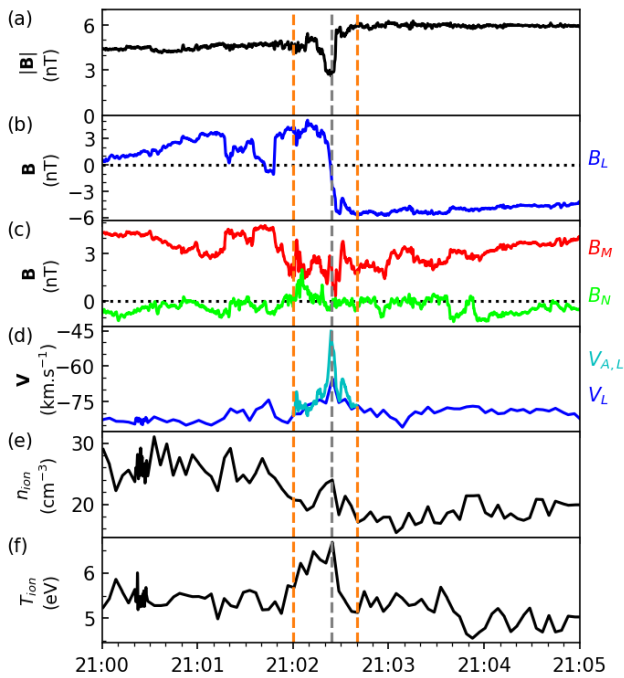


Fig. 5. Magnetic reconnection signatures at wave edge (3) in Fig. 4. (a) Magnetic field strength. (b) Magnetic field reconnecting L -component. (c) Magnetic field M, N components. (d) Ion bulk velocity V_L component with the predicted velocity jet ($V_{A,L}$; cyan). (e) Ion number density. (f) Ion temperature. Dashed orange lines mark the extent of the ion jet. A dashed grey line marks the maximum ion velocity during the jet.

V_L component in Fig. 5e. Note that the velocity data have lower cadence (4 s) than the magnetic field data (1 s), thus the velocity is sampled only at a few points in the vicinity of the current sheet interval. The velocity peak is marked by a grey dashed line. This ion jet has a magnitude of $\Delta V = 13 \text{ km s}^{-1}$. Although there is only one velocity measurement associated with the peak inside the jet, one should note that the operation cycle of the PAS instrument is such that each sample is made over only 1 s every 4 s. The measurement is thus made over a limited time exactly in the center of the current sheet, rather than over 4 s which would have led to significant time aliasing across the current sheet.

The change in B_L correlates with the change in V_L negatively on the inbound side and positively on the outbound side. This sequence of correlations is consistent with a jet that is produced by magnetic reconnection. Although we acknowledge that there is only one velocity measurement in the jet, there are additional signatures that are consistent with the interpretation of magnetic reconnection, such as the enhanced ion number density shown in Fig. 5e, consistent with mixing of ions from either side of the current sheet in the reconnection exhaust (Gosling et al. 2005) and the enhanced ion temperature consistent with plasma heating within the reconnection exhaust (Phan et al. 2014) in Fig. 5f.

To more quantitatively assess whether this jet is consistent with reconnection, we consider the Walén relation: $\Delta V_A \sim \pm \Delta \mathbf{B} / (\mu_0 m_p n_{ion})^{1/2}$, where + or - is applied for a positive or negative correlation between \mathbf{B} and \mathbf{V} , respectively, (Hudson 1970; Paschmann et al. 1986) within the exhaust as bounded by dashed orange lines in Fig. 5. The predicted jet velocity is shown as cyan in Fig. 5d. The predicted velocity produces a trend that resembles the observed jet. However, the predicted velocity jet from the Walén relation is estimated to be $\Delta V_A = 33 \text{ km s}^{-1}$. Thus,

the observed jet has a velocity that is 40% of the predicted jet velocity. A sub-Alfvénic reconnection jet is not unusual in observations. In the literature, sub-Alfvénic jet speeds are found when the spacecraft crosses the reconnection exhaust near the X-line. The development of secondary reconnection instabilities due to high plasma- β was also found to lower the reconnection jet speed (Haggerty et al. 2018). The presence of reconnection within KH waves may imply that it is produced as a consequence of vortex-induced-reconnection (e.g., Nykyri & Otto 2001; Nakamura et al. 2006; Karimabadi et al. 2013; Eriksson et al. 2016), which can be triggered when KH vortices develop and create thin current sheets between them. We further discuss this possibility in the discussion section.

3. Results

3.1. Linear theory analysis

To test whether the observed local conditions in Table 2 satisfy the KHI onset criterion, we consider the stability of a shear layer derived using the linear theory of Chandrasekhar (1961). The KHI onset criterion derived for an infinitely thin boundary layer in an incompressible plasma can be written (Hasegawa 1975) as

$$[\mathbf{k} \cdot (\mathbf{V}_1 - \mathbf{V}_2)]^2 > \frac{n_1 + n_2}{\mu_0 m_p n_1 n_2} [(\mathbf{k} \cdot \mathbf{B}_1)^2 + (\mathbf{k} \cdot \mathbf{B}_2)^2] \quad (1)$$

where \mathbf{k} is the wave vector, \mathbf{V} is the velocity field, \mathbf{B} is the magnetic field, and n is the ion number density, with the subscripts 1, 2 representing either side of the shear layer. The phase velocity of the KH mode, associated with the real part of the KH dispersion relation $V_{ph} = \omega/k$, where ω is the wave frequency and k is the wave number, is given as

$$V_{ph} = \frac{n_1 \mathbf{k} \cdot \mathbf{V}_1 + n_2 \mathbf{k} \cdot \mathbf{V}_2}{k(n_1 + n_2)} \quad (2)$$

The growth rate of the KHI, associated with the imaginary part of the dispersion relation, can be written as

$$\gamma = [\alpha_1 \alpha_2 [(\mathbf{V}_1 - \mathbf{V}_2) \cdot \mathbf{k}]^2 - \alpha_1 (\mathbf{V}_{A,1} \cdot \mathbf{k})^2 - \alpha_2 (\mathbf{V}_{A,2} \cdot \mathbf{k})^2]^{1/2} \quad (3)$$

where $\alpha_1 = n_1/(n_1 + n_2)$ and $\alpha_2 = n_2/(n_1 + n_2)$, and $\mathbf{V}_{A,1}, \mathbf{V}_{A,2}$ label the Alfvén speeds on either side of the boundary.

To simplify the configuration of the observed shear layer, we transform the velocity field using the application of the MVA technique to the ion bulk velocity from 20:14 to 21:50 UT. The maximum, intermediate, and minimum variance directions are found to be [0.53, 0.79, -0.32], [0.84, -0.53, 0.07], and [0.12, 0.31, 0.95], respectively. The ratios of the maximum to the intermediate eigenvalues (λ_1/λ_2) and the intermediate to the minimum eigenvalues (λ_3/λ_2) are 7.7 and 2.0, respectively, indicating reliable estimations (Siscoe & Sney 1972). The maximum variance direction is the direction where we find the velocity jump (i.e., the wave amplitude direction); it is assigned as Y . The minimum variance direction is the invariant direction; it is assigned as Z . The intermediate variance direction is the wave propagation direction; it is assigned as X . The transformed \mathbf{B} and \mathbf{V} are shown in Figs. 6a - 6d. The velocity jump is clearly seen in Fig. 6b with $\Delta V = 40 \text{ km s}^{-1}$. Fig. 6e shows a simplified configuration of this shear layer in the $X - Y$ plane. Note that the V_y and V_z are nearly constant and thus not shown in this figure.

We may calculate a KH growth rate from the simplified configuration in Fig. 6e. In this frame, the shear velocity is $\Delta \mathbf{V} = \mathbf{V}_2 - \mathbf{V}_1 \approx (40, 0, 0) \text{ km s}^{-1}$. Since the magnetic field

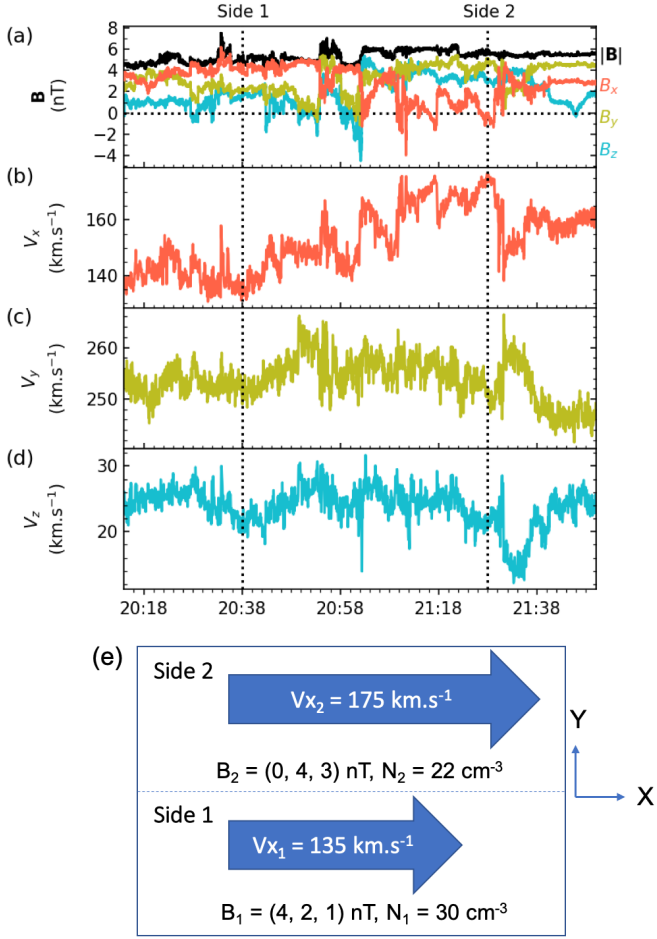


Fig. 6. Magnetic and velocity fields in the local shear frame obtained from the application of the MVA to the ion bulk velocity. (a) Magnetic field in the maximum (X), intermediate (Y), and minimum (Z) variance directions and its magnitude. (b, c, d) Velocity field in the X , Y , and Z directions, respectively. (e) Simplified shear boundary layer configuration obtained from the transformation to the maximum shear frame.

perpendicular to the shear direction, i.e., the B_z component (the invariant direction), does not impact the KHI (Chandrasekhar 1961), we can ignore this component. Assuming that the wave vector \mathbf{k} is in the $X - Y$ plane and makes an angle ϕ from the Y -direction such that $\mathbf{k} = (k \cos \phi, k \sin \phi, 0)$, Eq. 3 can be written as

$$\left(\frac{\gamma}{k}\right)^2 = \frac{\rho_1 \rho_2}{(\rho_1 + \rho_2)^2} \left[\Delta V_x \cos \phi + \Delta V_y \sin \phi \right]^2 - \frac{1}{\mu_0(\rho_1 + \rho_2)} \left[B_{1,x} \cos \phi + B_{1,y} \sin \phi \right]^2 - \frac{1}{\mu_0(\rho_1 + \rho_2)} \left[B_{2,x} \cos \phi + B_{2,y} \sin \phi \right]^2 \quad (4)$$

where $\rho_i = m_p n_i$, $i = 1, 2$. We find positive growth rates for an arbitrary angle ϕ with a maximum growth rate (γ/k) of 16 km s^{-1} . This means that the observed conditions of this event are unstable to the KHI. In brief, the linear theory analysis supports the KHI interpretation.

Assuming that the wave vector \mathbf{k} is in the same direction as the flow, we obtain the KH phase velocity from Eq. (2) to be $V_{ph} = 152 \text{ km s}^{-1}$. Since the average wave period from Table 1 is found to be $437 \pm 55 \text{ s}$ (7.3 ± 0.9 minutes), the KH wavelength

is estimated to be $\lambda_{KH} = 66,400 \pm 8,400 \text{ km}$ or 0.10 ± 0.01 solar radii. The linear theory analysis of a finite-thickness shear layer by Miura & Pritchett (1982a) predicts that the fastest growing mode occurs for $kL \sim 0.5 - 1.0$, where L is the initial shear layer thickness. Using $k = 2\pi/\lambda$, the fastest growing mode should have the wavelength of $2\pi L - 4\pi L$. Using our estimated λ_{KH} , we estimate the initial shear layer thickness to be $L \approx 5,300 - 10,500 \text{ km}$. Note that this estimate ignores any vortex merging or potential influence of pre-existing turbulence that could influence the size of the vortices that are observed.

3.2. KH simulation

To further test whether the observed conditions would support the KHI, we performed a numerical simulation using SoLO observations for Side 1 and Side 2 as boundary conditions. We exploit a numerical simulation that solves compressible MHD equations via a hybrid compact-weighted essentially non-oscillatory (WENO) scheme (Yang et al. 2016b). This hybrid scheme couples a sixth-order compact finite difference scheme for smooth regions and a fifth-order WENO scheme in shock regions, suitable for capturing strong discontinuities in MHD systems. The time stepping is performed by the third-order Runge-Kutta scheme. This code has been used to study compressible MHD turbulence (Yang et al. 2016a, 2017) and shear-driven turbulence by the KHI near the Sun (Ruffolo et al. 2020).

To simulate our event, we consider the local shear frame in Fig. 6e, derived in Section 3.1. Moreover, we consider the local KHI frame that travels with the KH phase speed at $V_{ph} \approx 150 \text{ km s}^{-1}$. In this frame, the speeds on Sides 1 and 2 are $U_{X,1} = -15 \text{ km s}^{-1}$ and $U_{X,2} = 25 \text{ km s}^{-1}$, respectively. Since the magnetic field perpendicular to the shear flow does not impact the KH growth (Chandrasekhar 1961), we only include magnetic field in the shear flow direction. The ion number density values on Sides 1 and 2 are $n_1 = 30 \text{ cm}^{-3}$ and $n_2 = 22 \text{ cm}^{-3}$, respectively. The ion temperature values on Sides 1 and 2 are set to $T_1 = 1.32 \text{ eV}$ and $T_2 = 3.63 \text{ eV}$, respectively. The ion β is set to 1. The magnetosonic Mach number across the shear layer is $\Delta U/c_{s,1} = 2.75$, where $\Delta U = 40 \text{ km s}^{-1}$ and $c_{s,1}$ is the sound speed on Side 1. The Alfvén Mach number is $\Delta U/V_{A,1} = 2.52$, where $V_{A,1}$ is the Alfvén speed on Side 1.

The numerical simulation is performed using a $L_x \times L_y = 8\pi \times 4\pi$ domain with $n_x \times n_y = 1024 \times 512$ resolution with periodic boundary conditions in the X -direction. For simplicity, equal viscosity and resistivity $\mu = \eta$ are used, i.e., the magnetic Prandtl number is set to unity. We solve the dimensionless form of the MHD equations by introducing several reference scales. The normalizations are $U_0 = 100 \text{ km s}^{-1}$, $n_0 = 30 \text{ cm}^{-3}$, $B_0 = 25 \text{ nT}$, and $T_0 = 66 \text{ eV}$. The simulation is 2-D as we ignore the invariant direction and only impose the magnetic field in the direction of the shear flow.

We set up double shear layers in the simulation domain similar to those of Ruffolo et al. (2020). The velocity and magnetic profiles are only set in the X -direction and both are colocated. The velocity profile is given by

$$u_x = U_\alpha \left[1 - \tanh\left(\frac{y - L_y/4}{d}\right) + \tanh\left(\frac{y - 3L_y/4}{d}\right) \right] + U_\beta, \quad (5)$$

where $U_\alpha = \left(\frac{U_1 - U_2}{2}\right)$, $U_\beta = \left(\frac{U_1 + U_2}{2}\right)$, $U_1 = -0.15U_0$, $U_2 = 0.25U_0$, and $d = 0.003L_y$ is the half thickness of the shear layer. The magnetic profile is given in a similar way as

$$B_x = B_\alpha \left[1 - \tanh\left(\frac{y - L_y/4}{d}\right) + \tanh\left(\frac{y - 3L_y/4}{d}\right) \right] + B_\beta, \quad (6)$$

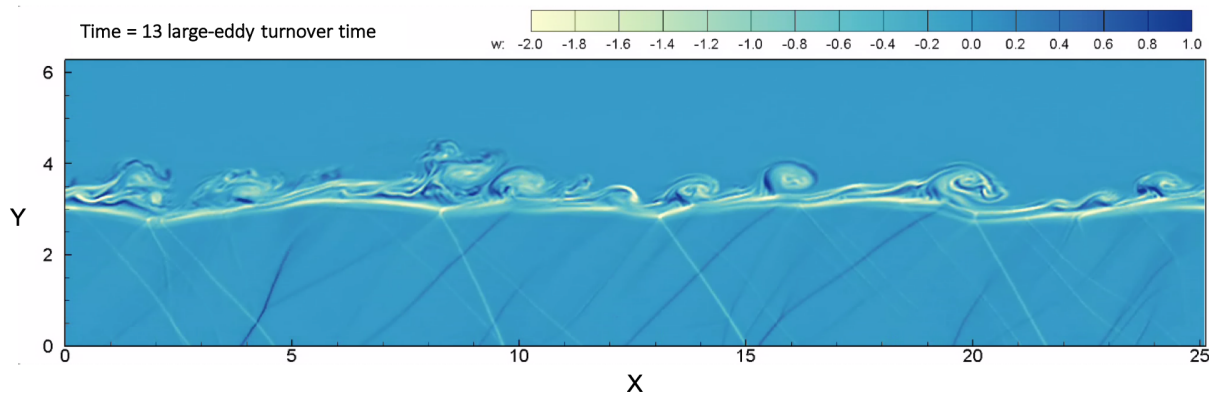


Fig. 7. A snapshot of the numerical simulation of the KHI using empirical values of the SoLO event from Side 1 and Side 2. The color-scale represents values of the out-of-plane flow vorticity (ω). The KHI quickly reaches the non-linear stage where rolled-up KH vortices form and coalesce. The stripes in vorticity in the lower part of the simulation are shocks produced by the supersonic flow as the Mach number ~ 3 (see text).

where $B_\alpha = \left(\frac{B_1 - B_2}{2}\right)$, $B_\beta = \left(\frac{B_1 + B_2}{2}\right)$, $B_1 = 0.16B_0$, and $B_2 = 0.0$. The density is set with $\rho_1 = \rho_0$ and $\rho_2 = 0.73\rho_0$ in normalized units. The initial temperature profile is set such that the total (magnetic plus thermal) pressure is balanced across the shear layer, where $T_1 = 0.02T_0$ and $T_2 = 0.055T_0$. Finally, the background shear is initially perturbed by adding a small compressive velocity field in the Y -direction in the form

$$du_y = \delta u_0 \left[e^{\left(\frac{y-L_y/4}{4d}\right)^2} - e^{-\left(\frac{y-3L_y/4}{4d}\right)^2} \right] \text{ran}(x)$$

where $\delta u_0 = 0.008(U_2 - U_1)$ (i.e., less than 10% of the shear flow magnitude) and $\text{ran}(x)$ represents a random number generator in the range $[-0.5, 0.5]$ at each grid value.

Fig. 7 shows a snapshot of the simulation at ~ 13 large-eddy turnover time for one of the shear layers (the two shear layer develop similar KHI structures). The color represents the flow vorticity (ω) in the out-of-plane direction. The KH waves are seen to develop in the simulation. They quickly reach the non-linear stage where rolled-up KH vortices clearly form (from ~ 6 large-eddy turnover times onwards) with visible vortex merging. This confirms that the solar wind observations by SoLO are consistent with the KHI growth. In the lower part of the simulation (Side 1), there are features seen as stripes in vorticity. These features are shocks that are produced by the supersonic flow on Side 1 (Mach number ~ 3) as the speed difference between the recirculating vortex and the nearby passing flow exceeds the sound speed (e.g., Landau & Lifshitz 1987). Future work ought to determine whether such features are sometimes observed in spacecraft data. For the present work, the key point would remain that the KHI does develop.

3.3. Boundary layer analysis

To understand local configurations of the KH waves, we characterize orientations of the observed wave edges in the RTN coordinates. In Fig. 4, the magnetic rotations are clearly defined for wave edges (2), (3), and (4). Fig. 8 shows \mathbf{B} and \mathbf{V} and their fluctuations from the average values between 20:35 and 21:20 UT. Wave edges (2) - (3), defined by clear rotations of \mathbf{B} in Fig. 8a and \mathbf{V} in Figs. 8d and 8e, are marked by cyan vertical dashed lines. We define these sharp rotations as the “outbound crossings”, which correspond to crossings of KH wave trailing edges that separate adjacent vortices. A KH trailing edge is typically

Table 3. Normal directions and orientations of the inbound (leading edge) and outbound (trailing edge) crossings with their normal directions (\mathbf{n}) and associated angle $\phi = \arctan(-n_T/n_R)$.

Wave edges	Times (UT)	Normal direction	Angle ϕ
Inbound (2')	20:49:20	[0.64, -0.57, -0.51]	41.7°
Outbound (2)	20:53:43	[0.78, -0.56, -0.28]	35.7°
Inbound (3')	20:58:08	[0.71, -0.63, -0.31]	41.5°
Outbound (3)	21:02:11	[0.91, -0.36, -0.21]	21.6°
Inbound (4')	21:06:50	[0.70, -0.68, 0.2]	44.2°
Outbound (4)	21:09:56	[0.58, -0.67, 0.45]	49.1°

thin, seen as a sharp transition, as a consequence of the compression between two waveforms or vortices. Smaller magnetic field rotations are also visible between these outbound crossings. We mark these smaller rotations as (2'), (3'), and (4') with magenta vertical dashed lines in Fig. 8. These edges show reverse transitions compared to the outbound crossings in B_R (red) and B_N (blue) components. We define these smaller transitions as “inbound crossings”, which correspond to crossings of KH wave leading edges. A KH leading edge is typically less sharply defined in in-situ data as it is in the vicinity of KH vortices that are regions of plasma mixing, so the transitions between two regions of the shear layer are less clear (e.g., Chen & Kivelson 1993; Fairfield et al. 2000).

To analyze the orientations of the wave edges, we calculate the boundary normals of the inbound and outbound pairs marked in Fig. 8. The normal of a discontinuity (i.e., current sheet) can be obtained from the cross-product of magnetic fields on either side of the discontinuity, i.e., $\mathbf{n} = \pm(\langle \mathbf{B}_1 \rangle \times \langle \mathbf{B}_2 \rangle) / |\langle \mathbf{B}_1 \rangle \times \langle \mathbf{B}_2 \rangle|$, where $\langle \mathbf{B}_1 \rangle$ and $\langle \mathbf{B}_2 \rangle$ are time averages of asymptotic magnetic fields before and after the current sheet interval, respectively. The obtained normal direction has a sign ambiguity (\pm); we assign a direction outward from the Sun, i.e., by forcing the radial component of \mathbf{n} to be positive. The time-averaged $\langle \mathbf{B}_i \rangle$, where $i = 1, 2$, are defined as 10-s averages of the magnetic fields. We obtain the normal orientations ($\mathbf{n} = [n_R, n_T, n_N]$) of the marked inbound and outbound crossings in Fig. 8. In addition, we define an angle $\phi = \arctan(-n_T/n_R)$ to be the angle of the current sheet normal from the R direction in the RTN coordinate system. The angle ϕ is in range $[-90^\circ, 90^\circ]$ where $\phi = 0^\circ$ is parallel to the Sun-SoLO line and $\phi = -90^\circ$ and 90° are perpendicular to the Sun-SoLO line in the T and $-T$ directions, respectively.

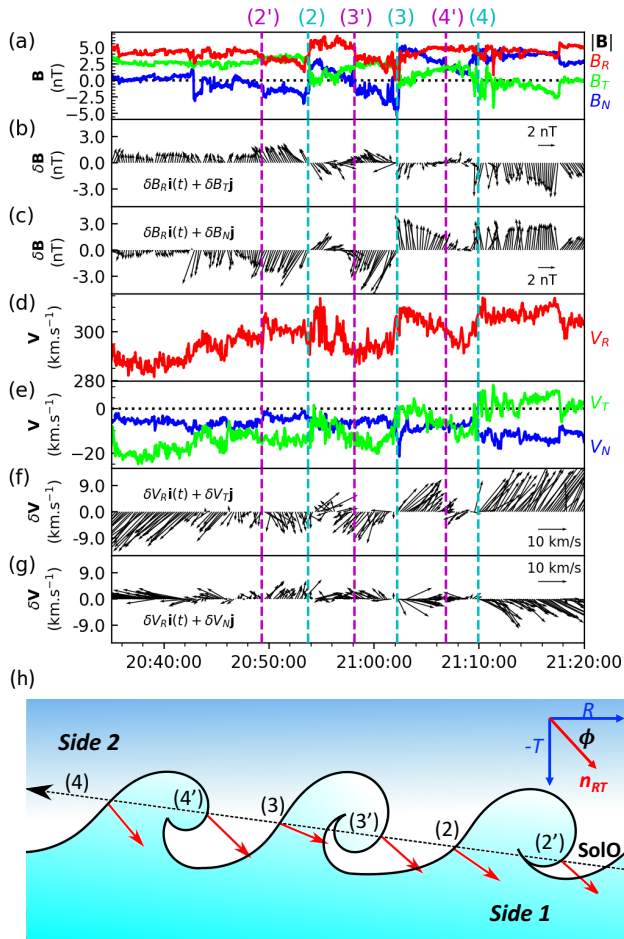


Fig. 8. SolO observations on July 23, 2020 with marked outbound and inbound crossings (i.e., wave edges) of the in-situ KH waves and a schematic sketch of the event. (a) Magnetic fields. (b, c) Magnetic field fluctuations from the averages in the $R-T$ and $R-N$ planes, respectively. (d) Ion bulk velocity V_R component. (e) Ion bulk velocity V_T and V_N components. (f, g) Velocity field perturbations in the $R-T$ and $R-N$ planes, respectively. Cyan dashed lines mark times of the outbound crossings, which correspond to KH trailing edges. Magenta dashed lines mark times of the inbound crossings, which correspond to KH leading edges. Normal directions of the inbound and outbound crossings are listed in Table 3. (h) Schematic sketch of the KH waves based on the normal angle (red arrows) at the wave edges.

Table 3 notes times of the inbound and outbound pairs, their normal directions (\mathbf{n}), and the normal angle ϕ . The normal directions for all inbound and outbound crossings are in between the R and $-T$ directions; these translate to the normal angles between 0° and 90° . The normal angles (ϕ) of an inbound-outbound pair were used to characterize in-situ waves at the Earth’s magnetopause by (Plaschke et al. 2016). By considering the angles of an inbound and outbound pair, we can determine whether the in-situ waveform is consistent with a sinusoidal wave, a KH wave, or another type of wave. Of particular relevance is that, when the waveform is a KH vortex (i.e., a rolled-up KH wave), the angles of the inbound and outbound pair should be in the same range (cf. Fig. 1 of Plaschke et al. (2016)). The observed angles of all the inbound-outbound pairs in Table 3 are well consistent with the steepening of KH vortices. This result supports the argument that the KHI is developed at the shear layer. We sketch the wave trains based on the normal angles with a hypothetical relative

Solo trajectory in Fig. 8h. Note that, in reality, the spacecraft is relatively static as the structures flow past with the solar wind.

To further see the vortex-type variations in \mathbf{B} and \mathbf{V} , we define their fluctuation vectors from the averages ($\delta\mathbf{B}$ and $\delta\mathbf{V}$) between 20:35 and 21:20 UT. Figs. 8b and 8c show $\delta\mathbf{B}$ in the $R-T$ and $R-N$ planes, respectively. Around the inbound crossing (3’), $\delta\mathbf{B}$ in the $R-N$ plane rotates smoothly in a clockwise sense. This pattern is also observed at other inbound crossings, although it is less pronounced. Figs. 8f and 8g show $\delta\mathbf{V}$ in the $R-T$ and $R-N$ planes, respectively. A clockwise pattern is also visible between (2) and (3’) in Fig. 8f. This pattern of rotation seen in both $\delta\mathbf{B}$ and $\delta\mathbf{V}$ is consistent with a vortical structure (i.e., a rolled-up KH vortex). The pattern is not as obvious at other inbound crossings; this may indicate that Solo does not pass centrally through the KH vortices in these cases.

3.4. Magnetic spectra

We now examine turbulence properties of the KH event. Fig. 9 shows the KHI interval with KH sub-regions V1 to V6 highlighted with colors (middle) together with time periods before and after the KH interval (see top). Fig. 9h shows a spectrogram of magnetic spectrum. The magnetic spectrum shows enhancement within the KH region compared to before or after the interval. The enhancement is visually strongest in V2 compared with other vortices. This V2 is the same interval as between (2) and (3’) in Fig. 8 where we see a clear clockwise rotation in the magnetic field and velocity field perturbations consistent with a rolled-up KH vortex. Thus, the strong enhancement in magnetic wave power provides evidence of enhanced activity in this vortex as plausibly facilitated by the development of a nonlinear KH vortex. The enhancement of the magnetic spectrum in V4 is also strong but less than for V2.

To quantitatively assess the magnetic field fluctuations in the full KHI region and in each of the six sub-regions V1-V6 marked in Fig. 9, we computed magnetic field spectra, which are shown in Fig. 10. Additionally, the KH-stable regions immediately before and after the KHI event are shown for reference. The vortex size is marked by an arrow (top left). The spectrum for the full KH region is shown in black while the spectra of the intervals before and after are shown in grey. As references, power law scalings of $k^{-5/3}$ (Kolmogorov 1941) at MHD scales and $k^{-2.8}$ at ion scales (i.e., Alexandrova et al. 2009) are plotted as black dashed lines. The scale of a thermal ion gyroradius (ρ_p) and an ion inertial length (d_p) based on the average properties in the KH region are marked with vertical solid and dashed black lines, respectively. The spectrum of the entire KH interval has more power than the intervals before and after, which both have similar low-intensity spectra. This suggests that the KHI is exciting additional fluctuations. The magnetic spectrum of the KH region approximately follows both power laws with a spectral breakpoint at $f \sim 0.2$ Hz. The spectrum essentially follows the power law $k^{-2.8}$ for scales smaller than the ion gyroradius. This indicates that the magnetic spectrum of the KHI interval is consistent with a classic turbulence cascade down to the kinetic scales (e.g., Bruno et al. 2014, 2017). This result provides evidence of shear-driven turbulence as driven by the local KHI.

Fig. 10 also shows magnetic spectra for individual vortices V1 - V6. Note that the compressed current sheets are excluded for the analyses of these vortices (this is why the colored regions are not exactly contiguous on Fig. 9). The powers of the magnetic spectra of all vortices are weaker than that of the entire KH region, indicating that the current sheets are key regions for enhancing the power spectrum. V2 (blue) and V4 (green) appear

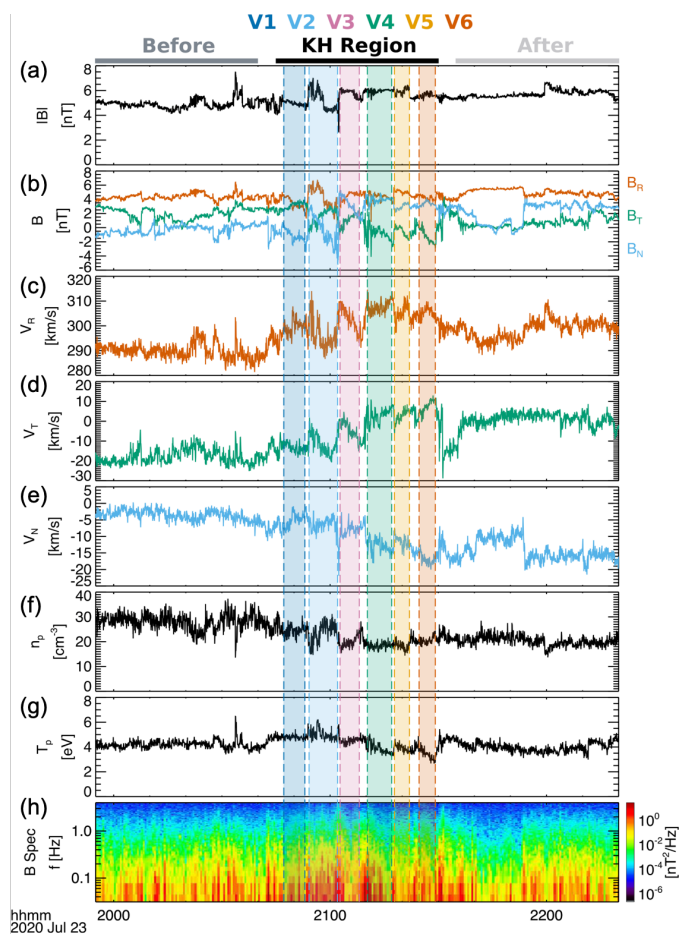


Fig. 9. Overview of the intervals for magnetic spectrum analysis. The KH region is marked in the middle (see top) together with the intervals before (top left) and after (top right). The KH vortices V1 to V6, marked between the compressed current sheets, are shaded in colors. (a) Total magnetic field. (b) Magnetic field in the RTN system. (c, d, e) Velocity field R , T , and N components, respectively. (f) Ion number density. (g) Ion temperature. (h) Magnetic spectrum.

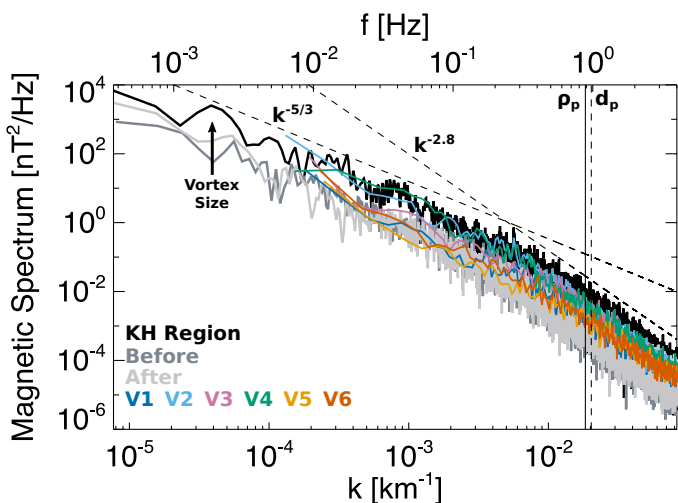


Fig. 10. Magnetic spectra of all regions marked in Fig. 9. The Kolmogorov power law $k^{-5/3}$ and the dissipation range scalings $k^{-2.8}$ are plotted for reference as straight black dashed lines. The vortex size is noted by an arrow (top left). The ion gyroradius scale (ρ_p) and the ion inertial length (d_p) are marked by vertical black solid and dashed lines, respectively.

to have higher powers compared to other vortices and almost reach the power of the entire KH region (black). The enhanced power in these vortices may be related to the excitation of turbulent fluctuations through secondary instabilities and the non-linear evolution of the KHI. The difference in the power spectrum between the different vortices may indicate that SolO was crossing different parts of KH vortices while crossing through the shear layer from Side 1 to Side 2. It is likely that SolO was passing through the center of a rolled-up vortex in V2, for reasons noted earlier. The lower powers of V1, V5, and V6 may indicate that SolO was skimming through the trough or crest parts of KH vortices. These results are in agreement with the assumed spacecraft trajectory through the KHI structure using the boundary layer analysis in Section 3.3.

4. Discussion

We have reported observations of the KHI within a shear layer embedded in the slow solar wind close to an HCS using Solar Orbiter. The event is observed in the inner heliosphere at a distance of ~ 0.69 AU. Despite several theoretical postulations (e.g., Parker 1963; Sturrock & Hartle 1966; Miura & Pritchett 1982a; Korzhov et al. 1984; Neugebauer et al. 1986; Hollweg 1987) and spacecraft missions in the inner heliosphere, direct evidences for the KHI were not reported in past in-situ observations of the solar wind. We discuss why this event may be favorable for a KHI detection as well as implications of the KHI in the solar wind as follows.

4.1. KHI criterion in the solar wind

First, we consider solar wind conditions that are favorable for the KHI. Based on the KHI onset condition (Eq. 1), the shear layer can more easily become unstable to the KHI when B is low and n is high because it requires a velocity jump across the shear layer greater than the local Alfvén speed ($\Delta V > V_A$). Near the Sun, B and V_A are typically large. This inhibitory effect on the KHI criterion should be stronger near the Sun. Nevertheless, there may be several situations where the local conditions allow the KHI. For example, remote sensing by DeForest et al. (2018) show a particularly strong shear values of a $\Delta V_R \sim 200$ km s $^{-1}$ across streamer structures in the young solar wind. Ruffolo et al. (2020) also propose the KHI development near the Alfvén critical zone, at $R < 0.17$ AU. The event we analyze here was observed near the HCS with many coherent structures and shears. Besides, this event is found in the slow wind, which is generally dense, making the conditions to meet the KHI criterion easier.

Second, we consider the magnetic and velocity field configurations across shear layers. The KHI is suppressed when \mathbf{B} is strong in the direction of $\Delta \mathbf{V}$ due to the stabilization by magnetic tension in the direction of the shear flow. In this interplanetary medium, we typically expect a shear interface along the Parker spiral direction (see Fig. 11) so \mathbf{B} may usually be aligned with $\Delta \mathbf{V}$. However, near the Sun, there may be velocity shear due to the solar-wind corotation with the Sun. Several studies have shown that the KHI may occur in various situations, i.e., at the edge of a CME (e.g., Foullon et al. 2013; Möstl et al. 2013) and at the interfaces between CME and sheath and between sheath and solar wind (e.g., Páez et al. 2017).

Third, Eq. 1 is derived by assuming an ideal MHD plasma with an infinitely thin shear layer. In reality, non-ideal MHD effects such as the compressibility can stabilize the KHI (e.g., Sen 1964); for example, the KHI only grows for a limited range of the velocity jump across a shear flow for a 1-D TD in homogeneous

plasmas and magnetic fields (e.g., Talwar 1964; Pu & Kivelson 1983). The solar wind is indeed compressible and thus we expect some stabilizing effects. In addition, shear layers have finite thicknesses. A finite thickness of the shear layer can also stabilize the KH mode for small wavelength perturbations (i.e., for large wave number k). A combination of the compressibility and the finite thickness can stabilize the KHI such that only certain modes of $k\Delta L$, where ΔL is the shear layer thickness, are KHI unstable (Miura & Pritchett 1982b). Although these two factors can impact the shear-layer stability, we do not expect their effects to be large, nor to be specifically dependent on distance from the Sun.

To summarize, there are factors that can impact the KHI development in the solar wind. The magnitude of B and V_A depend on distance from the Sun. As V_A is higher closer to the Sun, the KHI criterion should be more difficult to satisfy, except where the shear ΔV is particularly strong. Often \mathbf{B} may be parallel to the velocity shear, tending to inhibit the KHI, except in some circumstances, e.g., when there is a CME that changes the local conditions. Compressibility of the solar wind and a finite thickness of the shear region can help stabilize the KHI.

Since the observed conditions during our event are not particularly unusual for dense solar wind near the HCS, KHI development should not be rare. We now consider arguments related to KHI timescale and configuration as follows.

4.2. KHI timescale

A first fact to consider now is that when the KHI develops at a shear layer, it quickly reaches the non-linear stage (i.e., the rolled-up stage). The periodic features and vortical structures then get rapidly destroyed as the plasmas from either side of the shear layer mix and vortices coalesce. At such late stage, they would be indistinguishable from other solar wind types, albeit likely associated with higher levels of fluctuations as we have actually found in Section 3.4 for this event. The timescale for the decay of a KH vortex is on the order of one to a few eddy turnover time. The eddy turnover time of a KH vortex scales as a fraction of the KH wavelength (λ_{KH}) divided by the KH wave phase speed (V_{ph}). Assuming that the KH vortex size is about $\lambda_{KH}/3$ to $\lambda_{KH}/2$ (22,000 to 33,000 km) for the fastest growing mode (i.e., Walker 1981; Miura & Pritchett 1982a), with the $V_{ph} = 152 \text{ km s}^{-1}$ (see Section 3.1), we obtain a KH vortex turnover time of 2.4 to 3.6 minutes. Since the conditions of our event are not unusual for dense solar wind near the HCS, this short timescale for turnover time (before the vortex decay) may contribute to the rarity of KHI detection.

It is also possible that KH waves were detected by past missions but their signatures were not resolved. Several periodic oscillations in magnetic field strength were observed by Burlaga (1968) using the Pioneer-6 spacecraft, launched in 1965, at $\sim 0.8 \text{ AU}$. One of the cases considered was found to have sinusoidal $|\mathbf{B}|$ oscillations with a period of ~ 5 minutes, embedded in a velocity shear layer. Although no other fluctuations were seen in the data, it was suggested that these waves were generated by a KHI.

4.3. KHI configuration

When TDs form in the solar wind, they are typically at the boundary between solar wind flux tubes that move with relative velocity. Since the solar wind flux tubes bend following Parker spiral arcs to first order, we expect the normal of shear inter-

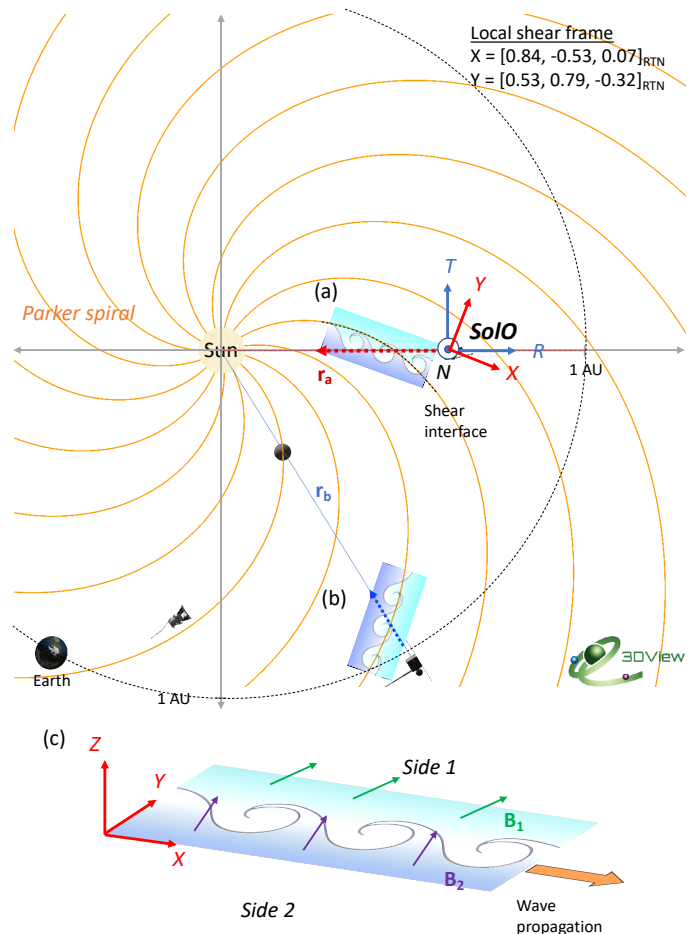


Fig. 11. (top) Schematic illustrations of scenarios for which the KHI develops (a) near SoLo position and (b) at 1 AU, shown in the ecliptic plane with the Parker spirals shown with orange solid lines (similar to Fig. 1). At (a), we project the derived $X - Y$ plane onto the $R - T$ plan as described in the text. The main flow is radially outward from the Sun as marked with vectors r_a and r_b . As the Parker spiral becomes more bent at (b), the spacecraft relative spacecraft trajectory is more perpendicular to the shear interface, making the likelihood of crossing several vortices much lower than in the inner heliosphere at (a). (bottom, c) A simplistic 3-D view of the KHI in (a) with the out-of-plane (Z) magnetic field shown with arrows on Sides 1 and 2, with corresponding values in Fig. 6e.

faces to be generally perpendicular to the Parker's spiral. Fig. 11 shows a schematic illustration of expected KHI configurations with respect to the solar wind Parker spiral in the ecliptic plane, produced using a constant velocity of 300 km s^{-1} close to the observed speed. We illustrate two scenarios of the KHI configuration (a) in the interplanetary medium between 0.3 and 0.7 AU and (b) near 1 AU. We describe a scenario for which the KHI develops relative to the Parker spiral based on our data as follows.

For our event at $\sim 0.7 \text{ AU}$ depicted at (a), we found that the velocity jumps for a displacement is in the direction $Y = [0.53, 0.79, -0.32]_{RTN}$ (the maximum variance direction of \mathbf{V}). This direction is indeed perpendicular to the Parker spiral, which is rather oriented along what we call the X direction, as shown at (a) (see frame definition in upper right part of the Fig. 11). The KH wave amplitude spreads in the Y direction as it is perpendicular to the shear interface. The wave propagation direction is $X = [0.84, -0.53, 0.07]_{RTN}$ (the intermediate variance direction

of \mathbf{V}). We expect that the KHI configuration in the solar wind will often be similar to this geometry. As explained next, such a KHI configuration relative to a more slowly moving spacecraft in the inner heliosphere impacts the likelihood of in-situ observations of the KHI.

We now consider two scenarios of KHI development (a) near SoLO position at ~ 0.7 AU and (b) near 1 AU in Fig. 11. As the main solar wind flow is in the radial direction, a static spacecraft at (a) would sample several vortices within the shear layer only if it has an appropriate relative trajectory through the layer. Note that SoLO was relatively static (with a speed of 11 km s^{-1}) compared to the KH wave phase speed (152 km s^{-1}). At a further distance from the Sun, i.e., near 1 AU as shown in (b), the Parker's spiral becomes more bent. The shear interface thus becomes more tilted relative to the outward solar wind flow as compared to the geometry observed at locations in the inner heliosphere (as show in Fig. 11a). Consequently, a spacecraft located in the inner heliosphere has a relative trajectory that makes it more likely to sample several vortices than a spacecraft that is farther out in the heliosphere, and which will make a more perpendicular cut across the shear layer, as depicted in Fig. 11b. This may be a prime explanation as to why despite the many spacecraft near 1 AU, there were no reports of in-situ KHI detection.

Note that the above considerations are based on a simplistic 2-D view. In reality, 3-D effects such as out-of-ecliptic magnetic and velocity fields can significantly impact the KHI configuration and development with respect to the Parker spiral. For example, we show magnetic fields perpendicular to the shear plane in Fig. 11c and these are in fact required to avoid the alignment of the velocity and magnetic shear, which otherwise has a stabilizing effect on the KHI. We acknowledge that our considerations are to first order only; future work should address this in more detail.

4.4. Implications of the KHI in the solar wind

The KHI is expected to play important roles, such as allowing for plasma mixing, generating turbulence, or producing Alfvénic fluctuations in the solar wind as mediated by KH vortex dynamics. During the present event, SoLO observed an ion jet consistent with magnetic reconnection (see Section 2.4). An interesting question is whether this reconnection is produced due to dynamics of a KH vortex. For vortex-induced reconnection (VIR), we expect reconnection to be produced at a thin current sheet in between two vortices. At the Earth's magnetopause, VIR jets were found to orient themselves along KH trailing edges (e.g., Eriksson et al. 2016) as the vortex evolves and further enhances the magnetic shear. In our case, we found that the jet is in the out-of-ecliptic direction while the KH trailing edges (see Table. 3) and the shear layer are in the R, T directions. Thus, it is unclear whether the observed jet is a VIR. We think that the N -directed jet is rather a consequence of the inclination of the local current sheet. Nevertheless, the KH vortex may further increase the magnetic shear at the KH edge and make the current sheet thin enough to trigger magnetic reconnection.

We now discuss the magnetic and velocity field fluctuations. We found that the KHI enhances fluctuations compared to outside the interval and the magnetic spectrum of the KHI region approximately follows the power law scalings of $k^{-5/3}$ and $k^{-2.8}$ at inertial and kinetic scales, respectively (Section 3.4). These enhanced fluctuations are consistent with turbulence generation by the KHI at the magnetopause (e.g., Stawarz et al. 2016; Nakamura et al. 2017). Therefore, the magnetic spectrum is consistent

with a classical turbulence cascade down to the kinetic scales. These observations are consistent with an enhancement of turbulence in the solar wind as driven by the local KHI (e.g., Goldstein et al. 1989). We also note that current sheets are key structures that contribute to the power spectrum, as power spectra of only vortex regions are lower than the overall spectrum. In addition, several of the vortices have enhanced power within them, which may be due to secondary instabilities, perhaps supporting the idea that the KHI helps to drive some fraction of the turbulent fluctuations in the solar wind.

One important implication of KHI in the solar wind is that it can contribute to the evolution of the magnetic and velocity fluctuations. Near the Sun, the KHI is believed to be a mechanism that leads to shear-driven turbulence at the Alfvén critical zone where $V = V_A$ and in the vicinity of the $\beta = 1$ surface (DeForest et al. 2016; Chhiber et al. 2018), leading to more isotropic solar-wind streams. Furthermore, the dynamical evolution invoked by shear-driven instabilities such as the KHI is found to be able to account for features observed by PSP including magnetic “switchbacks” near perihelia (Ruffolo et al. 2020). This topic needs to be investigated further but it is beyond the scope of the present study.

5. Conclusions

We report observations of the KHI with SoLO on July 23, 2020 at 0.69 AU, during the cruise phase. The KH waves are observed within the velocity shear layer with periodic fluctuations in several parameters in the slow solar wind near an HCS. Several KH waveforms are observed with a period of ~ 7 minutes but only a few vortices are clearly noticed. One of them is found to have magnetic and velocity field perturbations consistent with a rolled-up KH vortex in the non-linear stage. We test the observed conditions on either side of the shear layer with linear theory and find that the shear layer is indeed KHI-unstable. The maximum variance direction of the shear flow, associated to the KH wave amplitude direction, is found in the direction approximately perpendicular to the Parker spiral. The intermediate variance direction of the shear flow, associated with the net flow and thus the direction of the KH wave propagation, is along the Parker spiral. Using linear theory, the wave phase speed is estimated to be 152 km s^{-1} . The KH wavelength is approximately 66,400 km or 0.1 solar radii. We also confirm the local KHI development by exploiting a 2-D MHD simulation with the empirical values.

Additionally, we report the observation of an ion jet consistent with magnetic reconnection at one of the outbound (trailing) edges, likely as a result of current sheet compression in between two KH vortices. The ion jet has $\Delta V = 11 \text{ km s}^{-1}$ along the maximum variance direction, consistent with magnetic reconnection with a sub-Alfvénic jet. Nevertheless, we found other signatures consistent with magnetic reconnection, namely a drop in magnetic field strength, an ion number density enhancement (Gosling et al. 2005), and plasma heating (Phan et al. 2014). It is unclear whether this jet is produced due to KH vortex-induced reconnection (e.g., Nakamura et al. 2006) or the local inclination of the magnetic field, as the jet direction does not correspond to the KH trailing edge orientation (Eriksson et al. 2016).

We also report the enhancement of the magnetic and velocity field fluctuations within the KHI interval compared to intervals before and after. The power of the magnetic spectrum of the entire KHI interval approximately follows the power law scalings of $k^{-5.3}$ and $k^{-2.8}$ in the inertial and kinetic ranges, respectively, consistent with the turbulent cascade in the solar wind. This provides evidence for the local enhancement of turbulence as driven

by the KHI. Moreover, we find that current sheets within the KHI interval are key structures that enhance the power, as the magnetic spectra of individual KH vortices (excluding compressed current sheet intervals) generally have less power.

As our reported event here is an unambiguous in-situ observation of the KHI in the solar wind, we discuss possible reasons why the KHI was not reported in past in-situ observations. First, the KHI onset criterion requires a velocity jump across the shear layer that is larger than the local Alfvén speed ($\Delta V > V_A$) and weak magnetic field in the direction of the shear flow (i.e., low $\mathbf{B} \cdot \mathbf{V}$). Second, the KHI is estimated to quickly reaches the nonlinear stage where KH vortices roll up and merge. This timescale should be on the order of a few eddy turnover. The observed conditions are typical in the solar wind, and we estimate the timescale of the KHI to be on the order of minutes. In other words, when KHI develops in the solar wind, it evolves rapidly and is thus rather ephemeral. Third, the configuration in which the KHI develops may not be optimal for detection by a relatively slow-moving spacecraft near 1 AU owing to the geometry of the Parker spiral. The KHI develops at discontinuities formed in between solar wind flux tubes that move with a relative velocity. In this picture, the KH wave amplitude should spread in a direction perpendicular to the Parker spiral, albeit often with significant north-south components as in our case. Owing to its more skimming trajectory, a spacecraft in the inner heliosphere such as *Solo* may more easily pick up several waveforms in the shear layer. Further from the Sun, in contrast, the Parker spiral becomes more bent. A spacecraft near 1 AU is less likely to sample several vortices along its trajectory which has a larger angle to the discontinuity, making it difficult to recognize KH waves. We think these are main factors that contribute to the rarity of in-situ KHI detection in the solar wind.

This event provides evidence for the existence of the KHI in the solar wind. It sheds new light on solar wind shear processes in the interplanetary medium with direct applications to shear-driven turbulence mediated by the KHI, likely contributing to the solar wind fluctuations observed at 1 AU (e.g., Ruffolo et al. 2020). As the Alfvén speed decreases away from the Sun, the KH growth rate becomes higher (e.g., Neugebauer et al. 1986) and thus the KHI may be more common. Due to the short timescale of the linear KHI, there may be more chances to detect nonlinear KHI or its remnants. Recently, techniques for detecting kinetic features of the KHI during the nonlinear and turbulent stage of the KHI were proposed (Settino et al. 2021). Further studies would be needed to study secondary processes induced by the KHI such as vortex-induced reconnection and other kinetic mechanisms, as the KHI is rich with magnetic and plasma structures as is well known for the case of the magnetopause.

Acknowledgements. Work at IRAP was supported by the Centre National de la Recherche Scientifique (CNRS, France), the Centre National d'Etudes Spatiales (CNES, France), and the Université Paul Sabatier (UPS). Solar Orbiter data are publicly available at <http://soar.esac.esa.int/soar/>. We acknowledge science teams of the Connectivity Tool (<http://connect-tool.irap.omp.eu/>) and 3DView (<http://3dview.irap.omp.eu/>) at IRAP and CNES. Y. Y. is supported by grant No. 11902138 from the National Natural Science Foundation of China. The computing resources were provided by the Center for Computational Science and Engineering of Southern University of Science and Technology. D.R. is supported by grant RTA6280002 from Thailand Science Research and Innovation. J.E.S. is supported by the Royal Society University Research Fellowship URF\R1\201286. C.J.O. is funded under STFC grant number ST/5000240/1. Solar Orbiter Solar Wind Analyser (SWA) data are derived from scientific sensors which have been designed and created, and are operated under funding provided in numerous contracts from the UK Space Agency (UKSA), the UK Science and Technology Facilities Council (STFC), the Agenzia Spaziale Italiana (ASI), the CNES, the CNRS, the Czech contribution to the ESA PRODEX programme and NASA. Solar Orbiter SWA work at UCL/MSSL is currently funded under STFC grants ST/T001356/1 and ST/S000240/1.

References

- Alexandrova, O., Saur, J., Lacombe, C., et al. 2009, *Phys. Rev. Lett.*, 103, 165003
- Arge, C. N., Henney, C. J., Koller, J., et al. 2010, in *American Institute of Physics Conference Series*, Vol. 1216, Twelfth International Solar Wind Conference, ed. M. Maksimovic, K. Issautier, N. Meyer-Vernet, M. Moncuquet, & F. Pantellini, 343–346
- Axford, W. I. & McKenzie, J. F. 1992, in *Solar Wind Seven Colloquium*, ed. E. Marsch & R. Schwenn, 1–5
- Borovsky, J. E. 2008, *Journal of Geophysical Research (Space Physics)*, 113, A08110
- Bruno, R. & Carbone, V. 2005, *Living Reviews in Solar Physics*, 2, 4
- Bruno, R., Telloni, D., Delure, D., & Pietropaolo, E. 2017, *MNRAS*, 472, 1052
- Bruno, R., Trenchi, L., & Telloni, D. 2014, *ApJ*, 793, L15
- Burlaga, L. F. 1968, *Sol. Phys.*, 4, 67
- Burlaga, L. F. 1972, *Microstructure of the Interplanetary Medium*, ed. C. P. Sonett, P. J. Coleman, & J. M. Wilcox, Vol. 308, 309
- Burlaga, L. F., Lemaire, J. F., & Turner, J. M. 1977, *J. Geophys. Res.*, 82, 3191
- Chandrasekhar, S. 1961, *Hydrodynamic and hydromagnetic stability* (Clarendon Press, Oxford)
- Chen, S. H. & Kivelson, M. G. 1993, *Geophys. Res. Lett.*, 20, 2699
- Chhiber, R., Usmanov, A. V., DeForest, C. E., et al. 2018, *The Astrophysical Journal*, 856, L39
- De Pontieu, B., Title, A. M., Lemen, J. R., et al. 2014, *Sol. Phys.*, 289, 2733
- DeForest, C. E., Howard, R. A., Velli, M., Viall, N., & Vourlidas, A. 2018, *ApJ*, 862, 18
- DeForest, C. E., Matthaeus, W. H., Viall, N. M., & Cranmer, S. R. 2016, *The Astrophysical Journal*, 828, 66
- Eriksson, S., Lavraud, B., Wilder, F. D., et al. 2016, *Geophysical Research Letters*, 43, 5606
- Fairfield, D. H., Otto, A., Mukai, T., et al. 2000, *J. Geophys. Res.*, 105, 21,159
- Fairfield, D. H., Otto, A., Mukai, T., et al. 2000, *Journal of Geophysical Research: Space Physics*, 105, 21159
- Fargette, N., Lavraud, B., Rouillard, A. P., et al. 2021, forthcoming
- Foullon, C., Farrugia, C., Fazakerley, A., et al. 2008, *Journal of Geophysical Research (Space Physics)*, 113, A11203
- Foullon, C., Verwichte, E., Nakariakov, V. M., Nykyri, K., & Farrugia, C. J. 2011, *Astrophysical Journal Letters*, 729, 2
- Foullon, C., Verwichte, E., Nykyri, K., Aschwanden, M. J., & Hannah, I. G. 2013, *ApJ*, 767, 170
- Fox, N. J., Velli, M. C., Bale, S. D., et al. 2016, *Space Sci. Rev.*, 204, 7
- Génot, V., Beigbeder, L., Popescu, D., et al. 2018, *Planetary and Space Science*, 150, 111, enabling Open and Interoperable Access to Planetary Science and Heliophysics Databases and Tools
- Goldstein, M. L., Roberts, D. A., & Matthaeus, W. H. 1989, *Washington DC American Geophysical Union Geophysical Monograph Series*, 54, 113
- Gosling, J. T. & Phan, T. D. 2013, *Astrophysical Journal Letters*, 763, 1987
- Gosling, J. T., Skoug, R. M., McComas, D. J., & Smith, C. W. 2005, *Journal of Geophysical Research: Space Physics*, 110
- Haggerty, C. C., Shay, M. A., Chasapis, A., et al. 2018, *Physics of Plasmas*, 25, 102120
- Hasegawa, A. 1975, *Plasma instabilities and nonlinear effects*
- Hasegawa, H., Fujimoto, M., Phan, T.-D., et al. 2004, *Nature*, 430, 755
- Hickmann, K. S., Godinez, H. C., Henney, C. J., & Arge, C. N. 2015, *Sol. Phys.*, 290, 1105
- Hillier, A. & Polito, V. 2018, *ApJ*, 864, L10
- Hollweg, J. V. 1982, *Journal of Geophysical Research*, 87, 8065
- Hollweg, J. V. 1987, *ApJ*, 317, 918
- Hones, E. W., Birn, J., Bame, S. J., et al. 1981, *J. Geophys. Res.*, 86, 814
- Horbury, T. S., O'Brien, H., Carrasco Blazquez, I., et al. 2020, *Astronomy and Astrophysics*, 642, 1
- Hudson, P. D. 1970, *Planet. Space Sci.*, 18, 1611
- Kacem, I., Jacquy, C., Génot, V., et al. 2018, *Journal of Geophysical Research: Space Physics*, 1779
- Karimabadi, H., Roytershteyn, V., Wan, M., et al. 2013, *Physics of Plasmas*, 20, 012303
- Kieokaew, R., Lavraud, B., Foullon, C., et al. 2020, *Journal of Geophysical Research: Space Physics*, 125, 1
- Knetter, T., Neubauer, F. M., Horbury, T., & Balogh, A. 2004, *Journal of Geophysical Research (Space Physics)*, 109, A06102
- Kolmogorov, A. 1941, *Akademiia Nauk SSSR Doklady*, 30, 301
- Korzhev, N. P., Mishin, V. V., & Tomozov, V. M. 1984, *Planet. Space Sci.*, 32, 1169
- Landau, L. D. & Lifshitz, E. M. 1960, *Electrodynamics of continuous media*
- Landau, L. D. & Lifshitz, E. M. 1987, *Fluid Mechanics*
- Lepping, R. P. & Behannon, K. W. 1986, *J. Geophys. Res.*, 91, 8725
- Louarn, P. 2004, *Geophysical Research Letters*, 31, L19805
- Matthaeus, W. H. & Goldstein, M. L. 1982, *J. Geophys. Res.*, 87, 6011
- Miura, A. & Pritchett, P. L. 1982a, *Journal of Geophysical Research*, 87, 7431
- Miura, A. & Pritchett, P. L. 1982b, *Journal of Geophysical Research*, 87, 7431

- Möstl, U. V., Temmer, M., & Veronig, A. M. 2013, *The Astrophysical Journal*, 766, L12
- Müller, D., St. Cyr, O. C., Zouganelis, I., et al. 2020, *Astronomy and Astrophysics*, 642, 1
- Nakamura, T. K. M., Fujimoto, M., & Otto, A. 2006, *Geophys. Res. Lett.*, 33, L14106
- Nakamura, T. K. M., Hasegawa, H., Daughton, W., et al. 2017, *Nature Communications*, 8, 1582
- Neugebauer, M. 1985, *Journal of Geophysical Research*, 90, 6627
- Neugebauer, M. 2006, *Journal of Geophysical Research (Space Physics)*, 111, A04103
- Neugebauer, M., Alexander, C. J., Schwenn, R., & Richter, A. K. 1986, *J. Geophys. Res.*, 91, 13694
- Neugebauer, M. & Giacalone, J. 2010, *AIP Conference Proceedings*, 1216, 194
- Nykyri, K. & Otto, A. 2001, *Geophys. Res. Lett.*, 28, 3565
- Ofman, L. & Thompson, B. J. 2011, *ApJ*, 734, L11
- Øieroset, M., Phan, T. D., Drake, J. F., et al. 2019, *Geophys. Res. Lett.*, 46, 1937
- Owen, C. J., Bruno, R., Livi, S., et al. 2020, *Astronomy and Astrophysics*, 642
- Páez, A., Jatenco-Pereira, V., Falceta-Gonçalves, D., & Opher, M. 2017, *ApJ*, 851, 112
- Parker, E. N. 1958, *ApJ*, 128, 664
- Parker, E. N. 1963, *Interplanetary dynamical processes*.
- Paschmann, G., Papamastorakis, I., Baumjohann, W., et al. 1986, *J. Geophys. Res.*, 91, 11099
- Phan, T. D., Drake, J. F., Shay, M. A., et al. 2014, *Geophys. Res. Lett.*, 41, 7002
- Plaschke, F., Kahr, N., Fischer, D., et al. 2016, *Geophysical Research Letters*, 43, 7373
- Pu, Z.-Y. & Kivelson, M. G. 1983, *Journal of Geophysical Research*, 88, 841
- Roberts, D. A., Goldstein, M. L., Matthaeus, W. H., & Ghosh, S. 1992, *J. Geophys. Res.*, 97, 17115
- Roudier, T. & Muller, R. 1986, *Sol. Phys.*, 107, 11
- Rouillard, A. P., Pinto, R. F., Vourlidas, A., et al. 2020, *Astronomy & Astrophysics*, 642, A2
- Ruffolo, D., Matthaeus, W. H., Chhiber, R., et al. 2020, *The Astrophysical Journal*, 902, 94
- Sen, A. K. 1963, *Physics of Fluids (New York)*, 6
- Sen, A. K. 1964, *Physics of Fluids*, 7, 1293
- Settino, A., Perrone, D., Khotyaintsev, Y. V., Graham, D. B., & Valentini, F. 2021, *arXiv e-prints*, arXiv:2102.04117
- Siscoe, G. L. & Suey, R. W. 1972, *J. Geophys. Res.*, 77, 1321
- Sonnerup, B. U. Ö. & Cahill, L. J. 1967, *Journal of Geophysical Research*, 72, 171
- Stawarz, J. E., Eriksson, S., Wilder, F. D., et al. 2016, *Journal of Geophysical Research (Space Physics)*, 121, 11,021
- Sturrock, P. A. & Hartle, R. E. 1966, *Phys. Rev. Lett.*, 16, 628
- Talwar, S. P. 1964, *Journal of Geophysical Research*, 69, 2707
- Tsurutani, B. T. & Smith, E. J. 1979, *J. Geophys. Res.*, 84, 2773
- Walker, A. D. M. 1981, *Planetary and Space Science*, 29, 1119
- Yang, Y., Matthaeus, W. H., Shi, Y., Wan, M., & Chen, S. 2017, *Physics of Fluids*, 29, 035105
- Yang, Y., Shi, Y., Wan, M., Matthaeus, W. H., & Chen, S. 2016a, *Phys. Rev. E*, 93, 061102
- Yang, Y., Wan, M., Shi, Y., Yang, K., & Chen, S. 2016b, *Journal of Computational Physics*, 306, 73
- Zaqarashvili, T. V., Vörös, Z., & Zhelyazkov, I. 2014, *Astronomy & Astrophysics*, 561, A62